

PRECISION TRACKING SPACE SYSTEM (PTSS) INFRARED SENSOR THERMAL TESTING AND MODEL CORRELATION

Matt Felt, Brian Thompson, Lorin Zollinger
Space Dynamics Laboratory/Utah State University

Mike Marley, Ed Hawkins, Patrick Stadter
Applied Physics Laboratory/Johns Hopkins University

ABSTRACT

The Precision Tracking Space System (PTSS) was a constellation of infrared (IR) sensors planned by the US Missile Defense Agency (MDA) to observe and track ballistic missile objects in flight. The PTSS program funded testing to characterize the parasitic heat loads expected on the actively-cooled multi-band IR Sensor Assembly, a subassembly within the optical telescope, thereby reducing uncertainty in the cooler heat lift requirements and system power budget. A detailed flight-like thermal analog of the Sensor Assembly, including designed conductances, surface treatments, and multi-layer insulation, was tested in a fixture that simulated its flight interfaces with a controllable interface temperature. A heat flow sensor, located at the flight cold-head attachment point, provided heat lift measurements. Testing was performed with various boundary conditions and a least squares fit was used to discriminate between the conduction and radiation parasitic heat load components. This knowledge was used to correlate a detailed thermal model built in Thermal Desktop that could then be used to accurately predict flight heat lift and perform system level design trades. This document presents a detailed description of the testing, test results, model correlation methodology and results, and lessons learned.

BACKGROUND

PTSS was a constellation of satellites designed to provide persistent missile tracking over a large percentage of the Earth. Each satellite included an extremely capable remote sensing optical instrument known as the Optical Payload (OPL), and a Communications Payload to rapidly relay data between spacecraft in the constellation to a ground station. These sensors would provide persistent space-based coverage, increasing the nation's defensive capabilities against ballistic missiles both in theater and as part of homeland defense.

A coalition of partner labs consisting of National Labs and University Affiliated Research Centers was tasked with designing and manufacturing the first two prototypes of the PTSS sensors. These labs were to work together to design and test in flight a unit that could be passed to industry for completion of the constellation. While the partner labs were contracted to develop prototype sensors, no actual operational sensors were built. The majority of the information presented herein is basic research and none of the technical information qualifies for protection under applicable U.S. export control laws.

The notional OPL featured three Focal Plane Arrays (FPA) packaged in a Sensor Assembly, a three-mirror anastigmat Optical Telescope Assembly (OTA), and a state-of-the-art data processing unit to analyze the observations in real time. The Sensor Assembly and the telescope were both required to operate at cryogenic temperatures to meet the performance requirements. To achieve the required temperatures, two independent cryocoolers were to be used. One cooler would be used to cool the telescope to nominally 130-170 K and the other to cool the Sensor Assembly to nominally 70-80 K.

The heat loads to both of the cryocoolers were significant design parameters as they largely impacted system resources. The specific powers for the notional cryocoolers, meaning the amount of input power necessary to remove a unit of power from the object being cooled, were on the order of 20 to 25 W/W for the cold box cooler and 7-10 W/W for the telescope cooler. With the possibility of a significant impact on system level power, creating a thermal design to minimize heat loads on the coolers and performing tests to verify parasitic heat loads became of critical importance.

The notional PTSS OTA, a subassembly to the Optical Payload, is shown in Figure 1 with the Sensor Assembly thermal zone outlined in red. Several panels enclosing the Sensor Assembly have been hidden for clarity; cabling and Multi-Layer Insulation (MLI) are not shown. The Sensor Assembly is mounted within the telescope cavity that is controlled at a warmer temperature by a separate, dedicated cryocooler. Both thermal zones are designed to be virtually isothermal to minimize optical distortions. The testing and model correlation presented here focus on the notional Sensor Assembly.

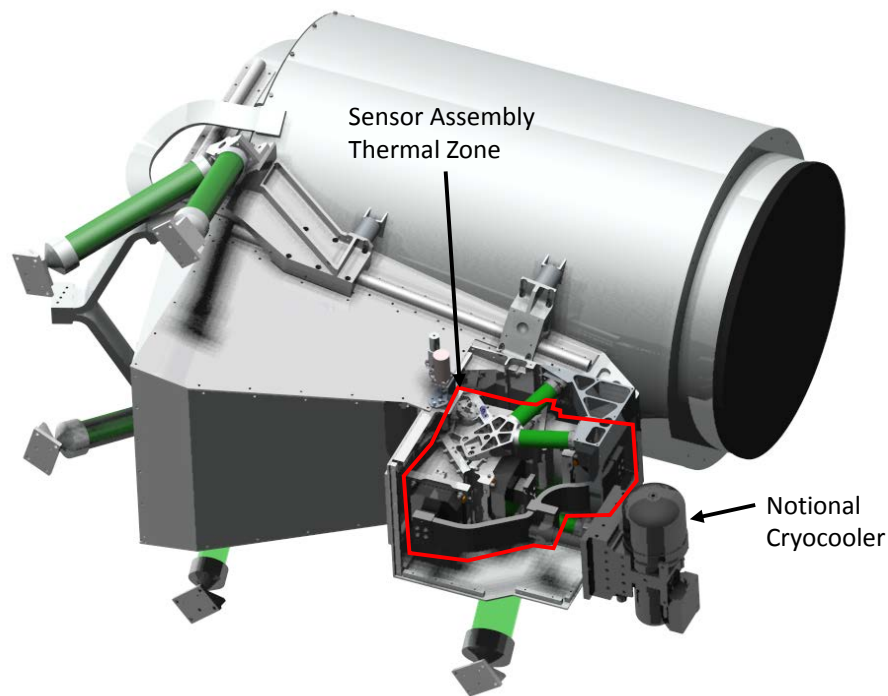


Figure 1. Notional PTSS OTA with Sensor Assembly thermal zone outlined in red.

SENSOR ASSEMBLY THERMAL ZONE DESCRIPTION

The notional three-channel Sensor Assembly is shown in Figure 2 with major components labelled. It is mounted to the warmer telescope structure on insulating G-10 bipods to minimize conductive heat transfer. It is cooled by a dedicated pulse-tube cryocooler that is connected to each FPA by a single trifurcated flexible thermal link. The isothermal telescope provides both the conduction and radiation boundary temperatures for the Sensor Assembly. Heat sources on the cold box include detector power dissipation, FPA cable parasitics (I^2R , conduction, and radiation), radiation from the warm telescope through MLI and into the Sensor Assembly aperture, conduction through bipod mounts, instrumentation and heater cable parasitics (I^2R , conduction, and radiation), and conduction through the shutter mechanism shaft.

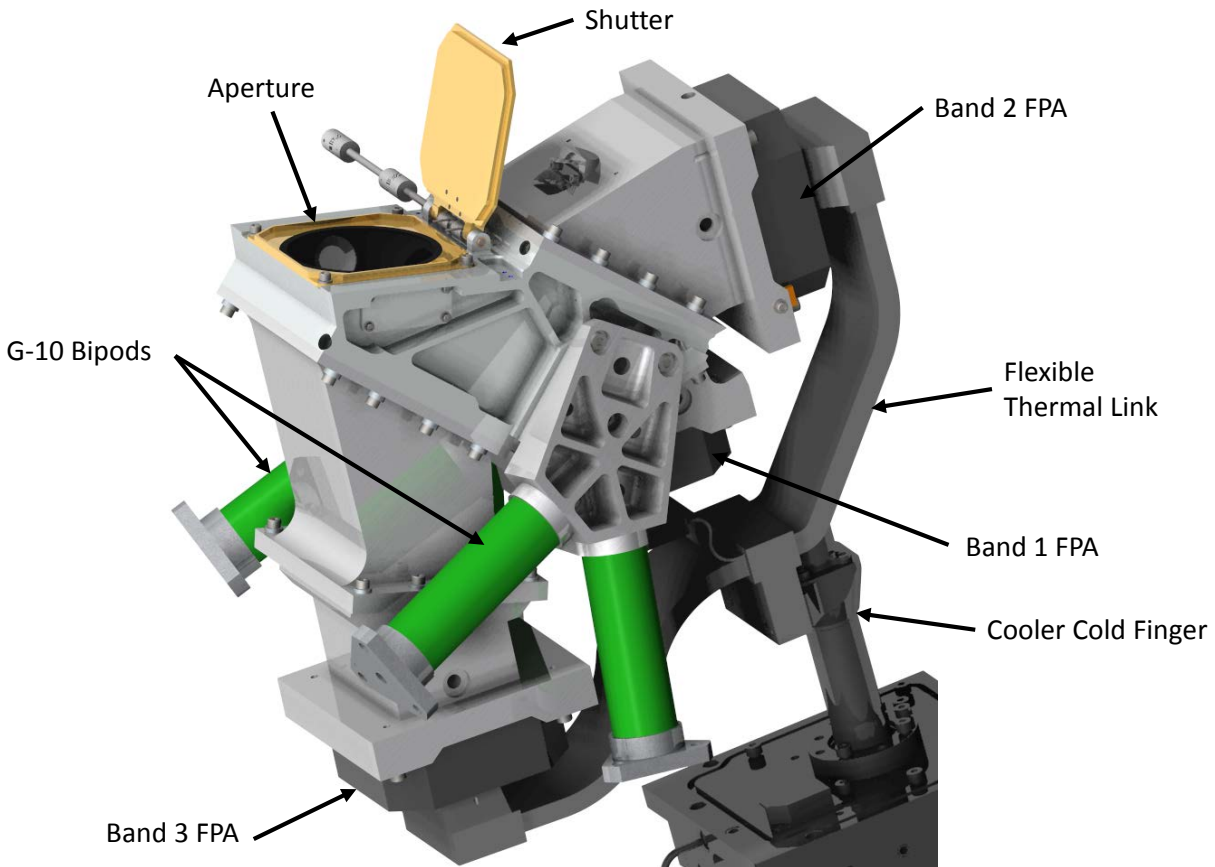


Figure 2. Notional Sensor Assembly with major components labelled (MLI and cabling not shown).

The notional Sensor Assembly is blanketed with MLI to minimize radiation heat loads. The notional MLI layup consists of 23 interior layers of 0.25 mil double-aluminized Mylar with one 0.5 mil single-aluminized glass-reinforced Kapton layer each on the top and bottom with the aluminized side facing out. Two layers of 190 mesh polyester netting maintain spacing between each layer. Each of the two primary blankets, one on the Sensor Assembly and one on the thermal link, is grounded in two places to comply with the program electromagnetic environment control plan. The outer layers of 5 smaller blankets (one on each G-10 tube and at

one place on the Sensor Assembly) are electrically connected to adjacent grounded blankets with a small wire at less than 1000 ohms. The complex shape of the thermal link required that the blanket be divided into three sets of 8-9 layers. Seams were offset for this blanket.

Edges of blankets were not sealed with the exception of those around the perimeter of the aperture. A simple Thermal Desktop model of an 8 in x 40 in blanket with edges sealed (outer layer connected to inner layer with 1 mil Kapton) showed a factor of two increase in heat transfer over an unsealed blanket given the same boundary conditions. Blankets were instead closed-out as shown in Figure 3.

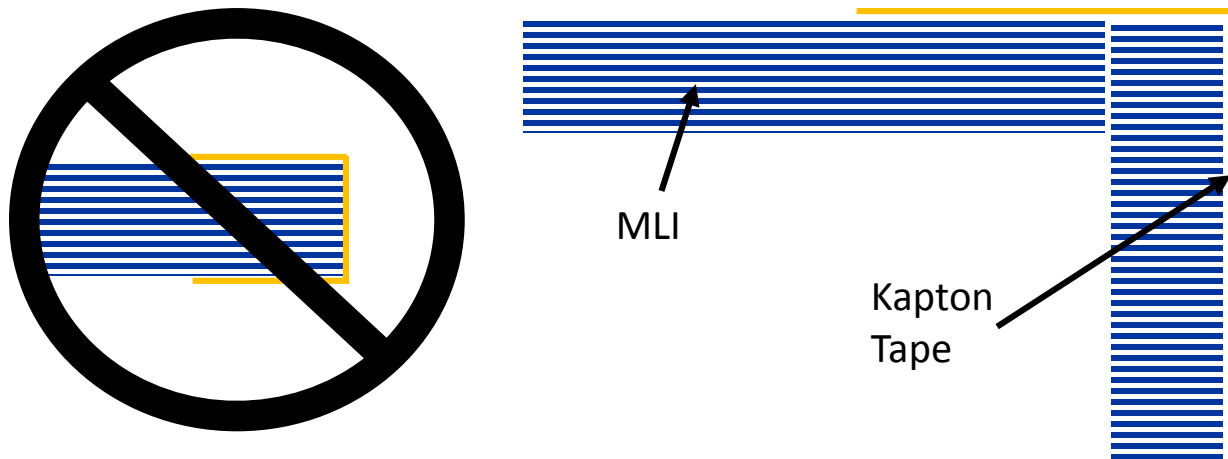


Figure 3. Notional MLI blankets are closed-out with no edge sealing except around aperture.

TEST OBJECTIVES

The PTSS program funded testing to characterize the parasitic heat loads onto the Sensor Assembly to reduce uncertainty in cooler heat lift requirements and therefore system power budgets. Additionally, a detailed thermal model of the Sensor Assembly built in Thermal Desktop was correlated to the data from this testing and used to extrapolate performance to non-tested conditions.

Another test objective was to evaluate the optical alignment stability of the Sensor Assembly with respect to the OTA through thermal cycling and after exposure to launch vibration environments. Optical flats were placed in various locations on the Sensor Assembly and a vacuum window was incorporated into the test setup to facilitate *in situ* alignment measurements. Some compromises were made in the thermal testing to meet this objective. Instead of exposing the entire Sensor Assembly to the simulated OTA environments, a portion of the Sensor Assembly, including the aperture, had to view a warm window. Details will be discussed in the next sections.

TEST ARTICLE DESCRIPTION

A flight-like Sensor Assembly structure was fabricated for this test. The primary structures and the insulating G-10 bipods were built exactly as designed. FPA design was still maturing so FPA thermal simulators were fabricated that included two independent sets of heaters to simulate active area power dissipation and cable parasitics. Cabling for heaters and temperature sensors was carefully sized to emulate the flight instrumentation cabling. The cables are spiraled down the G-10 tube to increase the length between thermal zones and reduce conducted parasitic heat. An image of the Sensor Assembly primary structures, FPA simulators, and temperature sensor and heater cables is shown in Figure 4. The fully blanketed assembly is shown in Figure 5 along with portions of the test fixture designed to emulate the OTA interface geometry and temperature.

The test also included the shutter mechanism that could be used to open and close the shutter. This allowed the shutter to be closed during thermal testing and opened briefly for optical alignment measurements to minimize test chamber effects on heat lift measurement.

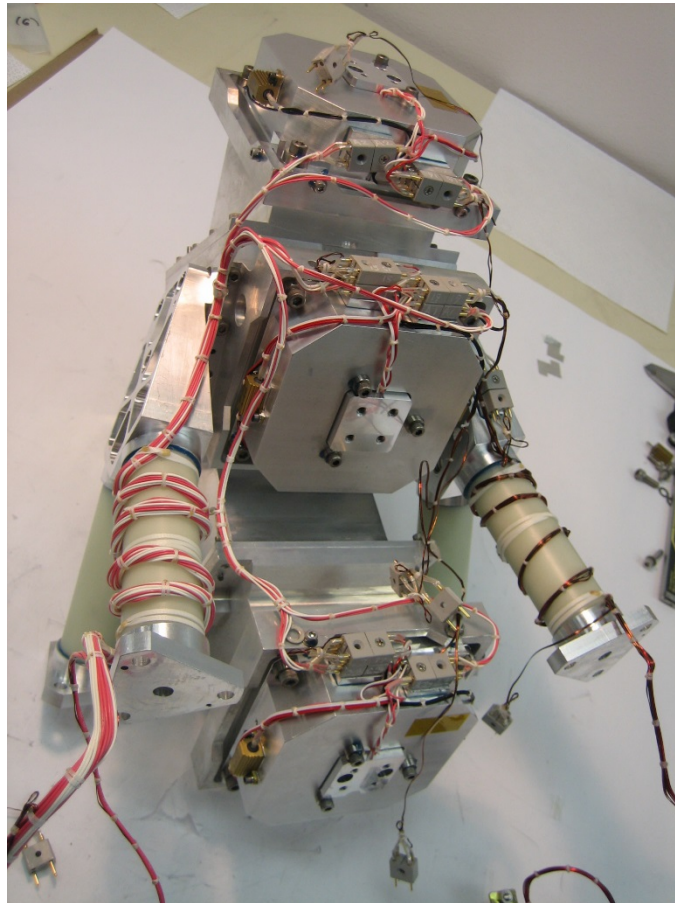


Figure 4. Sensor Assembly primary structures, FPA simulators, and cabling.



Figure 5. Fully blanketed Sensor Assembly during test fixture installation.

TEST EQUIPMENT

Vacuum Chamber

A 72 inch diameter chamber with an LN₂-cooled shroud and an optical window was selected for this test to ensure that both the optical and thermal objectives could be met. An independent test article heat exchanger provided the cold sink for thermal management of the Sensor Assembly and radiation enclosure. A flow-through heat exchanger was selected for this heat exchanger due to cost and schedule constraints. This independent cold sink allowed the Sensor Assembly to be mounted in a location to ensure a reasonable line of sight to the optical equipment for alignment testing. Figure 6 shows a CAD model section view of the test chamber with the Sensor Assembly installed. The LN₂-cooled chamber shrouding does not provide perfect coverage of the entire chamber. A section view of the thermal model showing warm surfaces in the chamber that could impact heat flow measurement is shown in Figure 7. These warm surfaces impact the test methodology and will be discussed later.

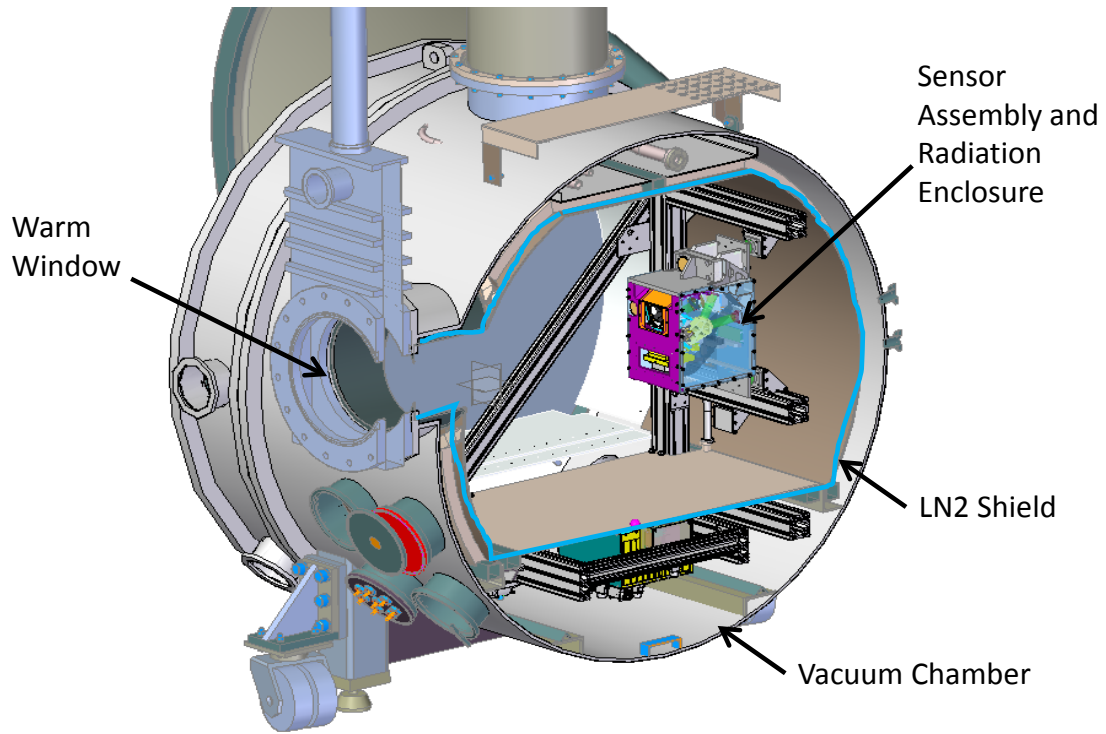


Figure 6. Section view of Sensor Assembly in vacuum chamber.

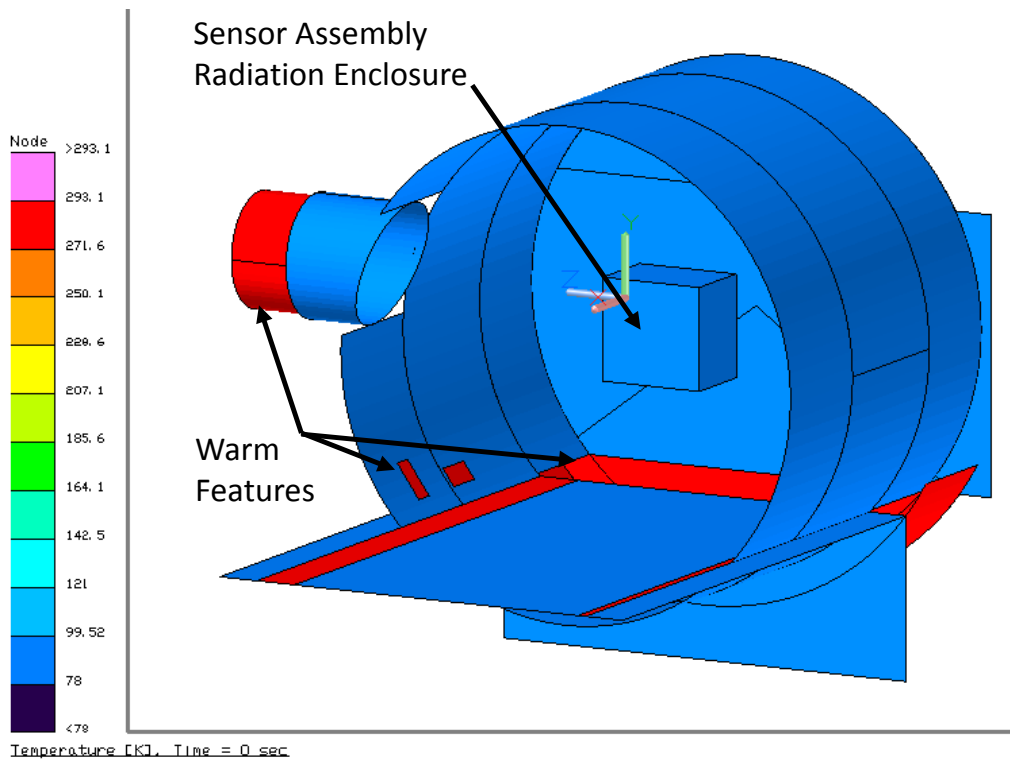


Figure 7. Vacuum chamber thermal model section view showing warm features.

OTA Interface Simulation

The LN2 heat exchanger was used as a temperature sink for the flexible thermal link connected to the Sensor Assembly. A fixture was designed to simulate both the geometry and the temperature of the OTA cavity that encloses the Sensor Assembly. The accurate OTA interface geometry helped discover and overcome MLI blanketing challenges and ensure that accurate effective emissivity measurements could be obtained.

The fixture was connected to the cold LN2 heat exchanger through carefully designed standoffs to ensure that the temperature could be controlled from 150 K to 215 K. A heater was placed on a thick aluminum structure near the standoffs to control temperature while minimizing fixture gradients. The fixture was blanketed with MLI to reduce heat transfer with the LN2-cooled shroud to further manage gradients. A Thermal Desktop model of the fixture predicted a gradient of about 1 K. A CAD model of the Sensor Assembly installed into the test fixture is shown in Figure 8. Note that the fixture provided the radiation environment for most of the Sensor Assembly except for the aperture and shutter. These components were exposed to the chamber thermal environment.

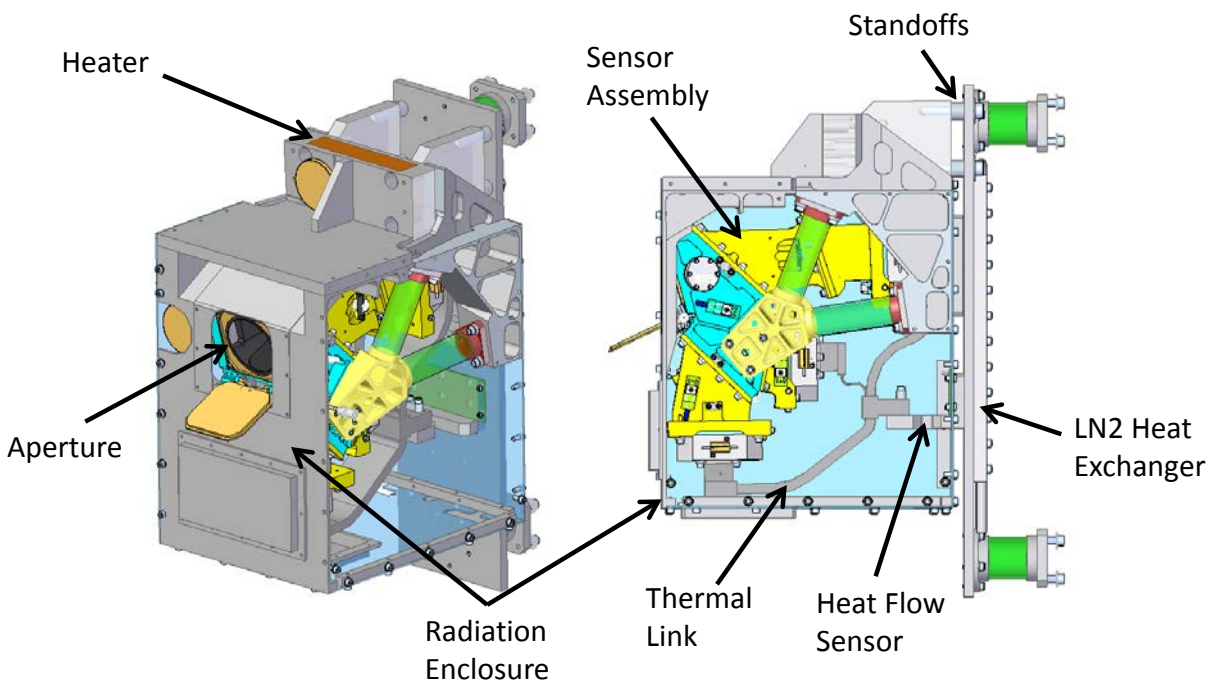


Figure 8. Sensor Assembly installed in test fixture.

Heat Lift Measurements

A heat flow sensor was placed between the thermal link and the heat exchanger to measure equivalent cryocooler heat lift as shown in Figure 8. This sensor was designed to a specific thermal conductance that was carefully chosen to optimize the gradient through the sensor at predicted test conditions. The gradient through the part was large enough that measurement errors became insignificant in comparison, but not so large that it drove the Sensor Assembly temperatures well above its operating temperature range. Model predictions for heat flow sensor gradients are shown in Figure 9. At a heat flow of about 1.3 watt, the gradient predicted through the restriction is about 2.4 K. Assuming both temperature sensors have 0.030 K error, this results in about 2.5% error in heat lift measurement.

Although it was calibrated, the thermal link could not be used to measure heat lift. The heat flow sensor was attached to the thermal link and both were calibrated simultaneously. The low gradients in the thermal link precluded it from being used as an effective heat flow sensor because the measurement error was significant compared to the total predicted heat flow. Link conductance was about 1 W/K and only one third of the heat flowed through each leg, translating to a heat lift measurement error of about 15%.

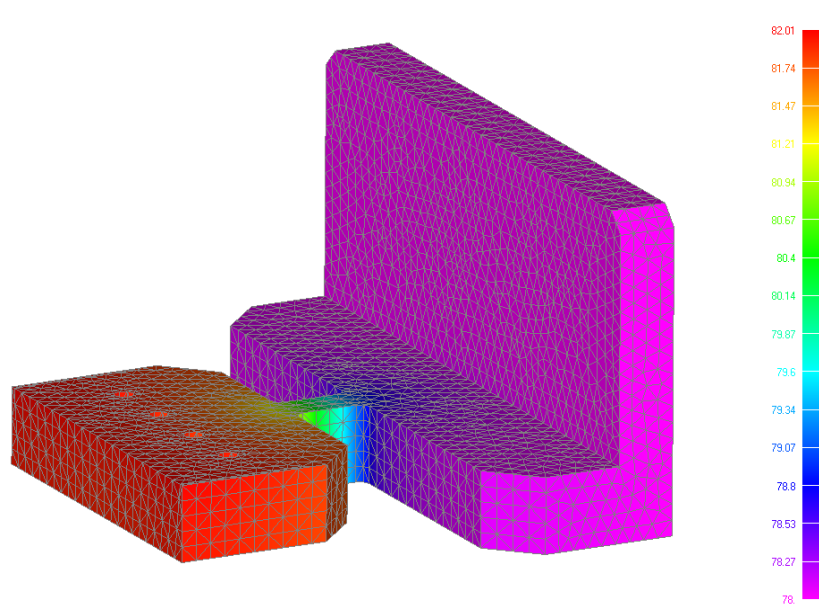


Figure 9. Heat flow sensor thermal model results.

LN2 Control

The test chamber LN2 shroud was cooled with a quiescent LN2 tank that was equipped with sensors and an auto-fill solenoid. This system was connected to the house LN2 supply and provided a very stable background requiring minimal maintenance. The flow-through heat exchanger was connected to a local LN2 supply Dewar. An additional Dewar was placed on the heat exchanger outlet to capture any excess liquid cryogen exiting the system. Both Dewars provided pressure relief valves to protect from over pressurization. The outlet of the exhaust-side Dewar was connected to a heater and a flow meter with a throttling valve to control flow and backpressure. A schematic of the LN2 control system for the flow-through heat exchanger is shown in Figure 10.

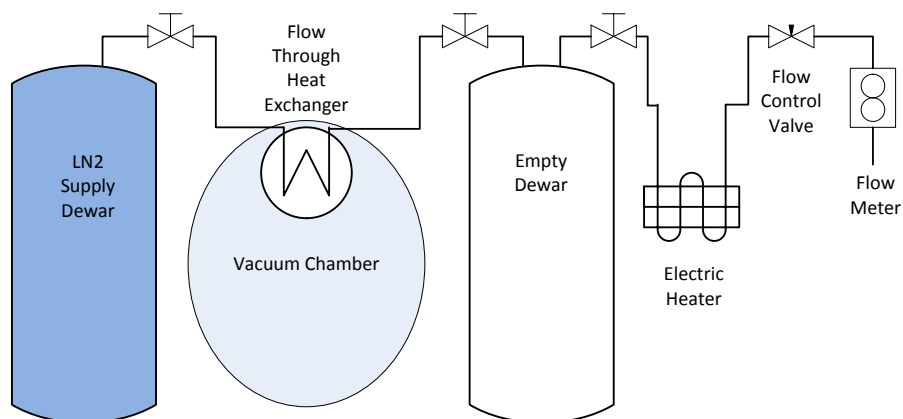


Figure 10. LN2 flow schematic.

TEST AND CORRELATION METHODOLOGY

A method was devised for discriminating between conduction and radiation heat transfer since both are unknowns in this test. This method required that boundary temperatures and heat flow be accurately measured under multiple thermal boundary conditions to accurately correlate the thermal model. This section discusses these in detail along with the parameters in the thermal model that are adjusted to correlate to the measured radiation and conduction heat transfer.

Discriminating Between Radiation and Conduction

The heat flow sensor provided the ability to accurately measure the heat lift required to maintain Sensor Assembly temperatures for a given set of test conditions. This data was used to correlate an existing Thermal Desktop model that can extrapolate results to untested conditions. The key to performing this correlation was the ability to discriminate between the radiative and conductive portions of heat transfer to adjust the parameters in the model to best match the test data. The model can be lumped into three thermal zones with conduction and radiation heat transfer occurring as shown in Figure 11.

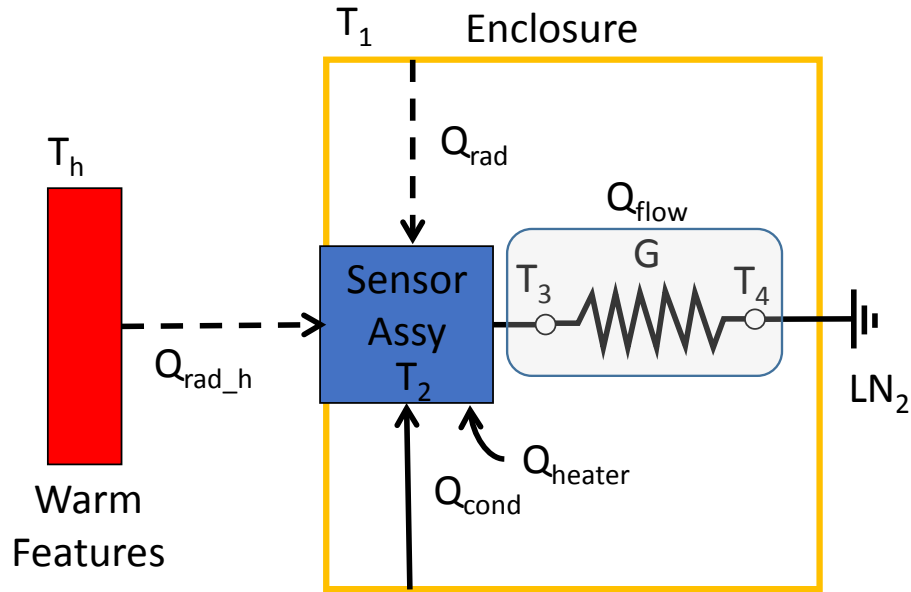


Figure 11. Lumped thermal diagram of test with solid arrows representing conduction and dashed arrows representing radiation heat transfer.

The heat flow through the heat flow sensor can be determined by

$$Q_{flow} = G(T_3 - T_4)$$

where G was experimentally determined in a calibration test. The thermal balance equation is defined as

$$Q_{flow} = Q_{heater} + Q_{cond} + Q_{rad} + Q_{rad_h}$$

Which can be expanded and rearranged as

Equation 1

$$Q_{flow} - Q_{heater} = A(T_1 - T_2) + B(T_1^4 - T_2^4) + C(T_h^4 - T_2^4)$$

Coefficient A represents the total conductance from the Sensor Assembly to the enclosure and consists of conductance through the G-10 mounts, conductance through the instrumentation wiring, and conductance through the shutter shaft. Coefficient B represents the total radiation heat transfer from the enclosure to the Sensor Assembly through MLI blanketed surfaces. Coefficient C represents the total radiation heat transfer from the warm components within the vacuum chamber to the Sensor Assembly which is dominated by the black aperture but also includes the shutter and adjacent gold-coated surfaces.

The coefficients A, B, and C are the only unknowns, with Q_{heater} and T_1 being controlled and the rest measured. Given three different test conditions, coefficients A, B, and C can be solved as a system of linear equations. Testing at four or more different temperatures allows the coefficients to be determined using a least squares fit. This provides the opportunity to compare the error at the test points to the best fit curve to evaluate the uncertainty associated with the results.

Equation 1 can be rewritten in Matrix form as follows:

$$M\hat{x} = b$$

Where

$$M = \begin{bmatrix} (T_1 - T_2)_1 & (T_1^4 - T_2^4)_1 & (T_h^4 - T_2^4)_1 \\ \vdots & \ddots & \vdots \\ (T_1 - T_2)_N & (T_1^4 - T_2^4)_N & (T_h^4 - T_2^4)_N \end{bmatrix} \quad \hat{x} = \begin{bmatrix} A \\ B \\ C \end{bmatrix} \quad b = \begin{bmatrix} (Q_{flow} - Q_{heater})_1 \\ \vdots \\ (Q_{flow} - Q_{heater})_N \end{bmatrix}$$

The least squares fit for the coefficients of interest is found by solving for the best fit x according to Equation 2.

Equation 2

$$\hat{x} = (M^T M)^{-1} M^T b$$

Temperature and Heat Flow Measurement

A Monte Carlo simulation of the least squares fit described above was generated to determine sensitivity to various measurements prior to testing. The test was most sensitive to the heat flow sensor temperature (T_3 and T_4 in Figure 11) measurement errors. Sensor Assembly and enclosure temperature (T_1 and T_2 in Figure 11) measurement errors of up to 0.5 K could be tolerated without significant impact on the test outcome. All temperatures were measured using calibrated thin-film platinum RTDs.

A critical part of minimizing heat flow measurement error is determining the no-load temperature offset between the temperature sensors in the heat flow sensor. This offset is applied to all subsequent measurements to eliminate this bias error from the measurement. This offset was determined during heat flow sensor calibration by allowing the part to reach a steady state temperature with no load on the system. This was easily accomplished since the part was well blanketed and fully enclosed in a cold shield during calibration. The heat flow sensor was calibrated using a different data acquisition system and different vacuum chamber than was used to conduct these tests.

Ideally this cold offset would be obtained in the full test configuration but it could not be accomplished in this case because a no-load condition could not be achieved. The primary

reason is that the vacuum chamber LN2 shrouding does not provide perfect coverage for the entire field of view of the aperture and shutter area exposed to the chamber. The view factor to warm features provided heat flow into the Sensor Assembly and prevented a true no-load offset from being obtained in this configuration. A few months prior to performing the full system test, the entire heat flow sensor test was submerged in LN2 to determine the no-load offset using the same data acquisition system and cabling to be used in the full system test. This offset was used to adjust the heat flow sensor gradients when calculating heat flow.

Thermal Model Correlation Methodology

An image of the Thermal Desktop model of the Sensor Assembly is shown in Figure 12. Once the best-fit coefficients were found, the thermal model was updated to match these coefficients. The total conductance term, coefficient A, was correlated by modifying the conductor representing the cables that connect the temperature sensors and heaters on the Sensor Assembly to the warm enclosure until the total conductance of all conductors in the thermal model matched the best-fit total conductance. Radiation between the enclosure and the Sensor Assembly, coefficient B, was correlated by adjusting the MLI e-star in the Thermal Desktop model and leaving the external surface emissivity at 0.05. No correlation was needed for coefficient C because, in the flight configuration, the aperture area of the Sensor Assembly views the black telescope cavity and was modeled accordingly.

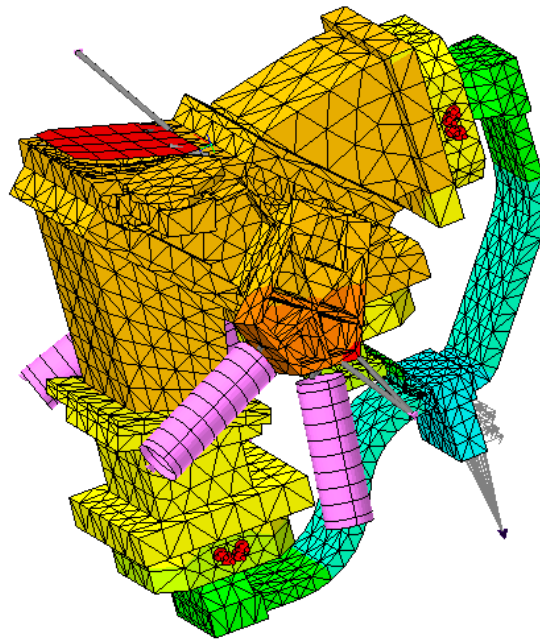


Figure 12. Thermal Desktop sensor assembly model.

TEST RESULTS

Tests were performed with the fixture temperatures nominally controlled at 155 K, 165 K, 205 K, and 215 K and with various power inputs into the Sensor Assembly at 205 K. A summary of

test results is shown in Table 1. Highlighted rows were not used in the least squares fit for determining the conduction and radiation coefficients for the following reasons. Test 0 was used for checking the thermal model of the chamber, but could not be used in the least squares fitting because the shutter was open. Test 5 was too noisy to be used in the least squares fit. A sample of useable test data from Test 4 is shown in Figure 13 through Figure 15. The average temperatures used in calculations are also plotted showing the times over which the temperatures were averaged.

The data for Test 5 was discarded due to the noise in the heat exchanger as shown in Figure 16. The noise was a result of the low LN2 flow rate through the system. In an effort to achieve the lowest possible heat exchanger temperature and to conserve LN2, the flow from the supply Dewar was restricted as much as possible. As the flow approached the minimum required to dissipate the heat on the system, these fluctuations were observed. This noise was also present on the heat flow sensor causing a large uncertainty in the heat flow measurement and leading to exclusion from the least squares fit calculations.

Table 1. Test Data Summary (Reference Figure 11)

Test	Description	T ₁ Avg. Enclosure Temp (K)	T ₂ Avg. Sensor Assy Temp (K)	Q _{flow} Measured Heat Flow (W)	Q _{heater} Total Applied Heat (W)	Q _{flow} - Q _{heater} (W)
0	Cold Offset, Open Shutter	84.270	82.048	0.2046	0.0	0.2046
1	Cold Offset, Closed Shutter	84.308	81.819	0.1064	0.0	0.1064
2	155K No Load	153.984	84.368	0.8184	0.0	0.8184
3	165K No Load	164.708	85.374	0.9736	0.0	0.9736
4	205K No Load	203.536	86.653	1.6650	0.0	1.6650
5	215K No Load	213.181	86.445	1.8613	0.0	1.8613
6	205K 1.5W	202.617	91.529	3.1869	1.4888	1.6980
7	205K 3.0W	202.601	97.528	4.6121	2.9658	1.6463
8	205K 4.5W	202.646	102.393	6.1566	4.4517	1.7049

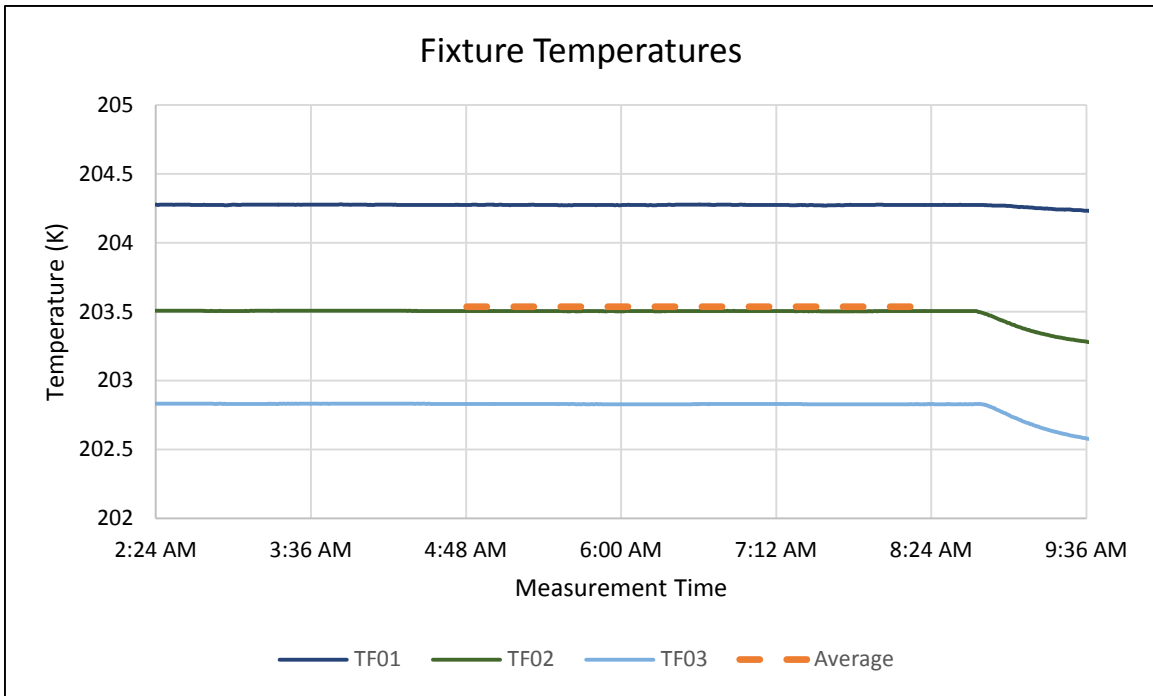


Figure 13. Fixture temperatures for Test 4.

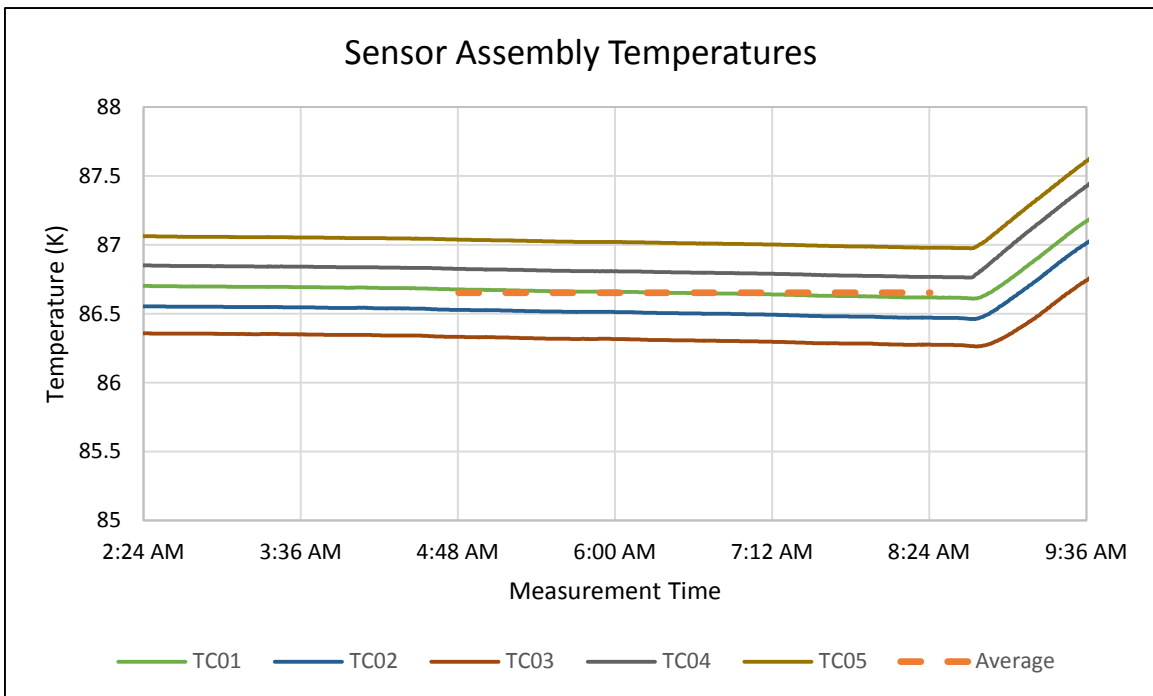


Figure 14. Sensor assembly temperatures for Test 4.

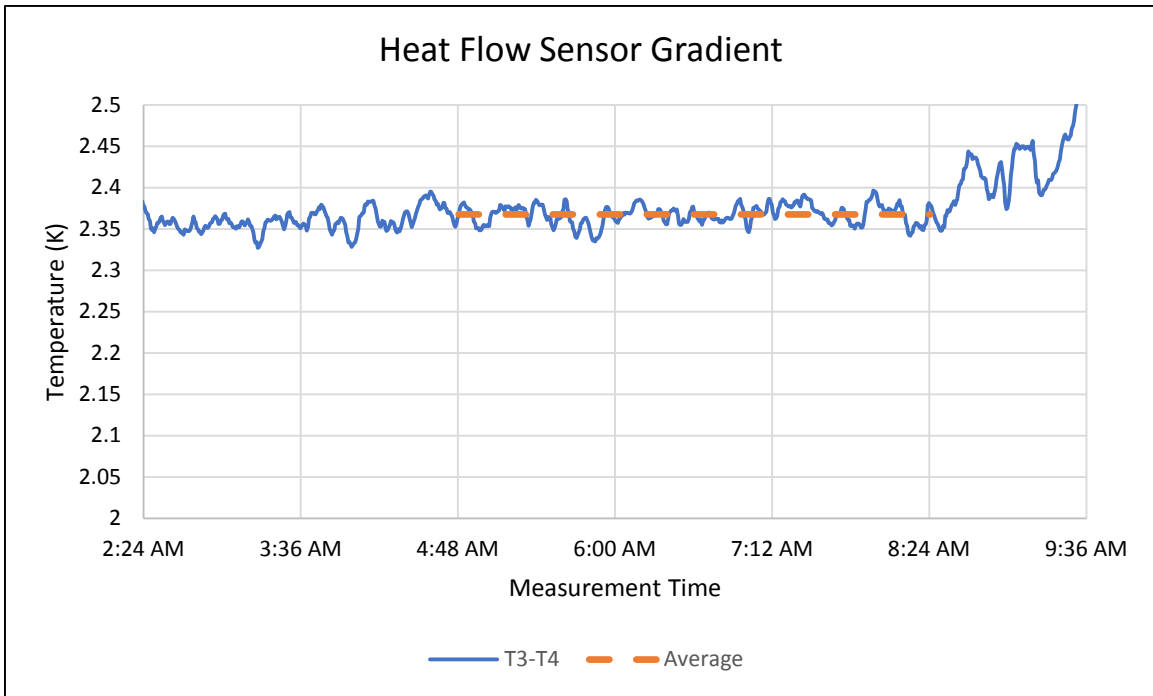


Figure 15. Heat flow sensor gradient test results for Test 4.

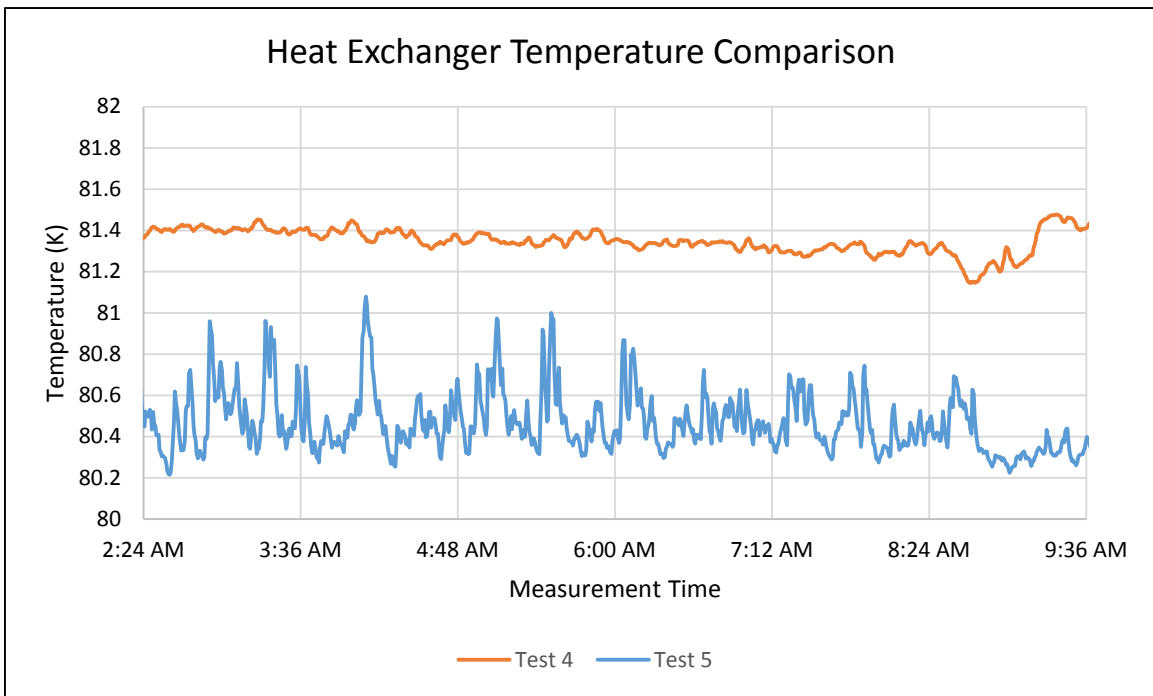


Figure 16. Heat exchanger temperature noise for Test 5 compared to Test 6.

THERMAL MODEL CORRELATION RESULTS

The test data in Table 1 (except for the highlighted rows) was input into Equation 2 to solve for the coefficients A, B, and C shown in Equation 1. Once these coefficients were obtained, the best estimate for heat lift was calculated using the test data as input. This was compared to the actual measured results for those same data points to estimate the error in the best fit approximation. Error plots versus each input are shown in Figure 17. The largest estimated error was less than 100 mW, 6% of the total for that test.

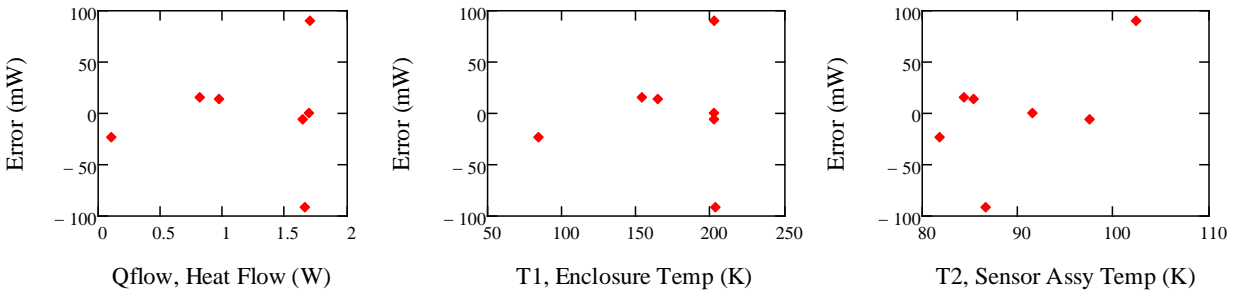


Figure 17. Best-fit results error versus test variable.

An MLI e-star of 0.053 in the thermal model correlated to within less than 1% of calculated radiation heat loads using the best-fit coefficient B. This is slightly higher than the pre-test assumed e-star in the model of 0.04. With external MLI surface emissivity (ϵ_{ext}) modeled as 0.05 in Thermal Desktop, the total effective emittance (ϵ_{tot}) of the blanked surface was calculated to be 0.026 according to Equation 3. This is very close to the original assumption of 0.022. The conductance of the cabling conductor was reduced by a factor of 0.94 to correlate the conduction coefficient. Heat maps for the correlated thermal model are shown for the two extreme enclosure temperatures in Figure 18 and Figure 19.

Equation 3

$$\epsilon_{tot} = \left(\frac{1}{\epsilon_{ext}} + \frac{1}{estar} \right)^{-1}$$

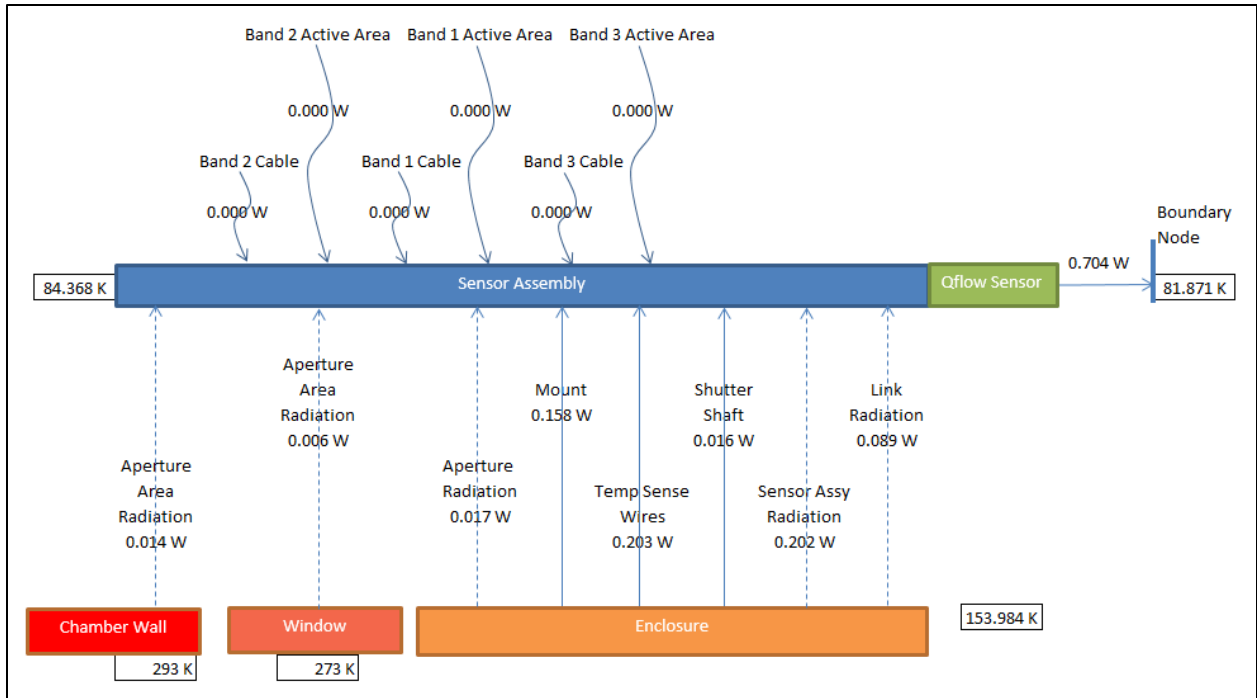


Figure 18. Heat map for Test 2.

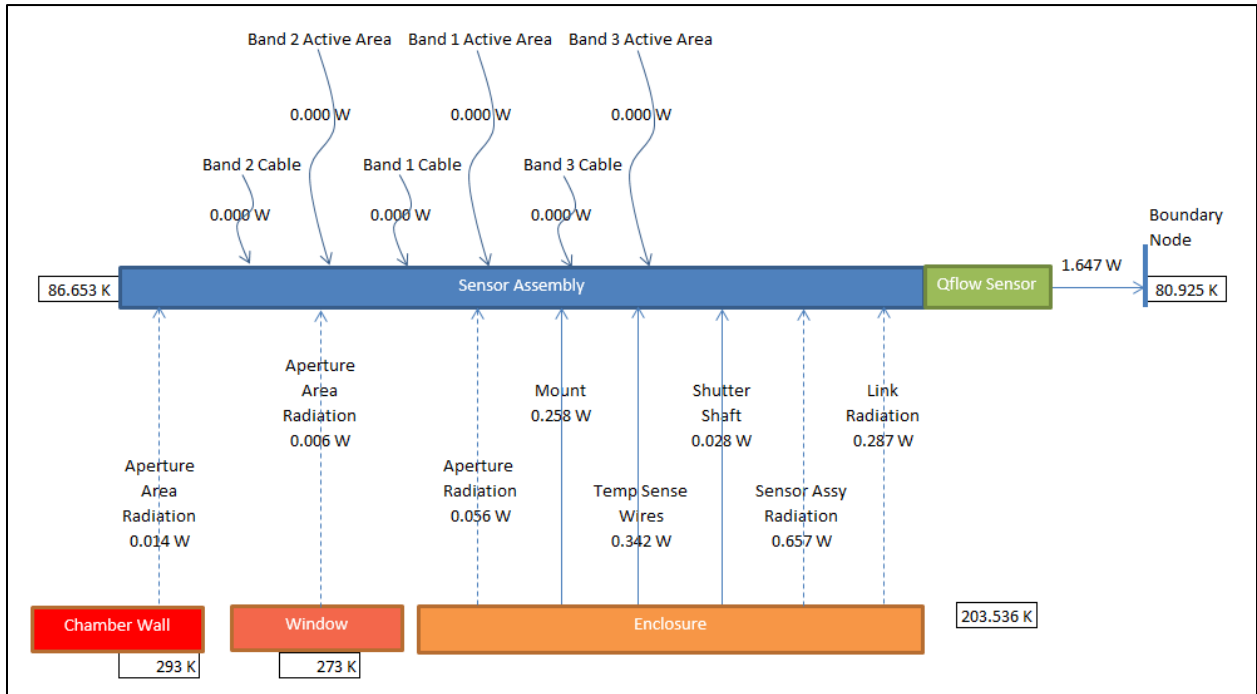


Figure 19. Heat map for Test 4.

LESSONS LEARNED

Significant test time was lost due to flow stability issues and temperature settling times caused by the flow-through LN2 heat exchanger. Furthermore, some test data had to be discarded due to excessive temperature noise. A small investment in a quiescent LN2 tank for a heat sink instead of the flow-through heat exchanger would have greatly simplified the testing process, resulted in higher quality data, and ultimately saved the program money.

The thermal compromises made to allow optical test objectives to be met were overcome with the modeling correlation efforts described herein. If greater accuracy were needed in the thermal testing, the optical portion of the test could have been omitted and the thermal testing would have been simpler and more accurate. Specific items that would have been improved include being able to obtain an accurate heat flow sensor offset and being able to simulate the exact thermal environment for the Sensor Assembly, including the Sensor Assembly aperture. Both thermal and optical test objectives were met with this test.

CONCLUSIONS

The conductance and e-star estimates for the PTSS Sensor Assembly were successfully determined by testing at multiple temperatures and performing a least-squares fit on the data. In addition to reducing uncertainty at the tested conditions, this provided for accurate model correlation for extrapolation to untested conditions. The cable conductance was within 6% of the expected value. The MLI e-star was slightly higher than predicted. The correlated total effective emittance falls within the expected range given the complexity of the geometry and blanketed surface area as shown in Figure 20.

This test was very successful at reducing uncertainty in cryocooler heat lift requirements. The original thermal model predictions were quite accurate, with the total parasitic loads falling within 10% of the correlated thermal model. Although some thermal compromises were made to meet optical test objectives, both test objectives were successfully met.

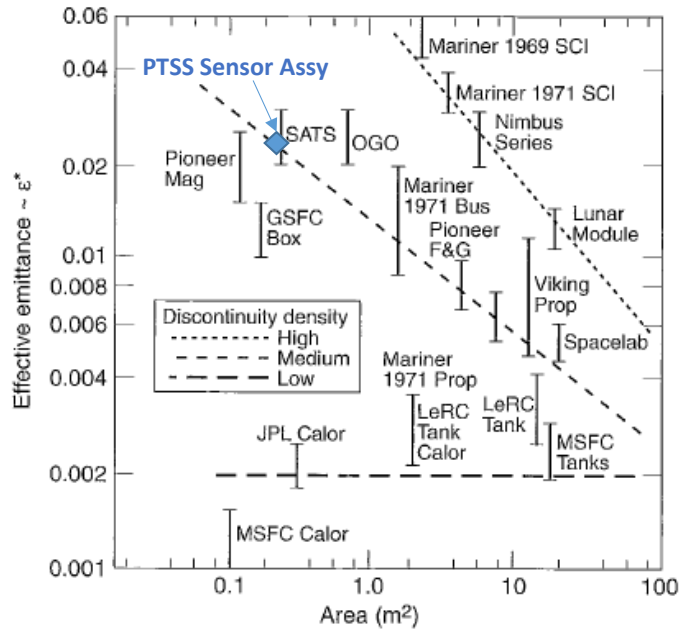


Figure 20. Effective emittance compared with historical blanket performance.¹

CONTACT

Matt Felt
 PTSS Optical Telescope Assembly Lead Thermal Engineer
 Space Dynamics Laboratory
 1695 North Research Park Way
 North Logan, UT 84341
 Phone (435)-713-3389
matt.felt@sdl.usu.edu

Brian Thompson
 PTSS Optical Telescope Assembly System Engineer
 Space Dynamics Laboratory
 1695 North Research Park Way
 North Logan, UT 84341
 Phone (435)-713-3358
brian.thompson@sdl.usu.edu

Lorin Zollinger
PTSS Optical Telescope Assembly Program Manager
Space Dynamics Laboratory
1695 North Research Park Way
North Logan, UT 84341
Phone (435)-713-3326
lorin.zollinger@sdl.usu.edu

Mike Marley
The Johns Hopkins University Applied Physics Laboratory
11100 Johns Hopkins Road
Laurel, MD 20723-6099
Phone (443) 778-5735
ed.hawkins@jhuapl.edu

S. Edward Hawkins, III
The Johns Hopkins University Applied Physics Laboratory
11100 Johns Hopkins Road
Laurel, MD 20723-6099
Phone (443) 778-2270
michael.marley@jhuapl.edu

Patrick A. Stadter
The Johns Hopkins University Applied Physics Laboratory
11100 Johns Hopkins Road
Laurel, MD 20723-6099
Phone (443) 778-4658
patrick.stadter@jhuapl.edu

NOMENCLATURE, ACRONYMS, ABBREVIATIONS

A	Total conductance from Sensor Assembly to warm OTA
B	Total radiation heat transfer coefficient through Sensor Assembly MLI, or effective $\sigma \cdot \epsilon \cdot \text{Area}$
C	Total radiation heat transfer coefficient from warm chamber components to Sensor Assembly, or effective $\sigma \cdot \epsilon \cdot \text{Area}$
CAD	Computer Aided Design
FPA	Focal Plane Array
G	Conductance of heat flow sensor
IR	Infrared
I^2R	Joule heating
LN2	Liquid nitrogen
MDA	Missile Defense Agency
MLI	Multi-Layer Insulation
OPL	Optical Payload
OTA	Optical Telescope Assembly
PTSS	Precision Tracking Space System
Q_{cond}	Total Sensor Assembly conductive parasitics, $A \cdot (T_1 - T_2)$
Q_{flow}	Heat flow from Sensor Assembly to LN2 sink (see Figure 11)
Q_{heater}	Total applied heat to Sensor Assembly (see Figure 11)
Q_{rad}	Total Sensor Assembly radiative parasitics through MLI, $B \cdot (T_1^4 - T_2^4)$
Q_{radh}	Total Sensor Assembly radiative parasitics from warm components to aperture Aperture area, $C \cdot (T_h^4 - T_2^4)$
T_1	Enclosure temperature (see Figure 11)
T_2	Sensor Assembly temperature (see Figure 11)
T_3	Heat flow sensor hot side temperature (see Figure 11)
T_4	Heat flow sensor cold side temperature (see Figure 11)
T_h	Temperature of warm features in vacuum chamber (see Figure 11)
σ	Stephan-Boltzmann constant

¹ David G. Gilmore, editor, *Spacecraft Thermal Control Handbook Volume I: Fundamental Technologies*, (El Segundo: The Aerospace Press; Reston: American Institute of Aeronautics and Astronautics, Inc., 2002), 165, figure 5.4. Reprinted with permission of The Aerospace Corporation.